Konrad-Zuse-Zentrum
für Informationstechnik Berlin

Takustraße 7
D-14195 Berlin-Dahlem
Germany

PETER DEUFLHARD AND MARTIN SEEBASS

Adaptive Multilevel FEM as Decisive Tools in the Clinical Cancer Therapy Hyperthermia

Preprint SC 98-30 (November 1998)

Adaptive Multilevel FEM as Decisive Tools in the Clinical Cancer Therapy Hyperthermia

Peter Deuflhard and Martin Seebass[1]

Konrad–Zuse–Zentrum für Informationstechnik Berlin
Takusstr. 7, D-14195 Berlin, Germany.
e–mail: {deuflhard,seebass}@zib.de

1 Introduction

The paper surveys recent progress in a joint mathematical-medical project on cancer therapy planning. Within so-called *regional hyperthermia* the computational task is to tune a set of coupled radiofrequency antennas such that a carefully measured tumor is locally heated, but any outside *hot spots* are avoided. A mathematical model of the whole clinical system – air, applicator with antennas, water bolus, individual patient body – involves Maxwell's equations in inhomogeneous media and a parabolic bioheat transfer equation, which represents a simplified model of heat transfer in the human body (ignoring strong blood vessel heat transport). Both PDEs need to be computed fast and to medical reliability (!) on a workstation within a clinical environment. This requirement triggered a series of new algorithmic developments to be reported here, among which is an adaptive multilevel FEM for Maxwell's equations, which dominates the numerical simulation time. In total, however, the main bulk of computation time (see Table 3 in Section 4 below) still goes into segmentation – a necessary preprocessing step in the construction a 3D *virtual patient* from the input of a stack of 2D computed tomograms (left out here).

[1]supported by Deutsche Forschungsgemeinschaft, Sonderforschungsbereich 273

2 Linear versus Nonlinear Heat Transfer Model

In a phased array applicator the antennas are grouped into k channels that can be independently controlled. For each channel j the amplitude a_j and phase delay θ_j can be set. For convenience we define complex amplitudes

$$z_j = a_j \; exp(-i\theta_j) \qquad j = 1, \ldots, k \tag{1}$$

The aim is to determine an optimal set of complex amplitudes for each individual patient.

Bio–Heat–Transfer Equation. The heat transfer model used in our simulations is the bio–heat–transfer (BHT) equation originally proposed by Pennes [16]

$$\rho c \, \frac{\partial T}{\partial t} = \operatorname{div}(\kappa \operatorname{grad} T) - c_b W (T - T_b) + Q_e \; , \tag{2}$$

where ρ is the density, c and c_b are specific heat of tissue and blood, κ is the thermal conductivity; T_b is the blood temperature; W is the mass flow rate of blood per unit volume of tissue, the so-called perfusion; $Q_e = \frac{1}{2}\sigma \mid \mathbf{E} \mid^2$ is the electromagnetic power density deposited in tissue; σ is the electric conductivity of tissue, and $\mathbf{E}$ is the electric field.

The BHT equation describes the heat transport by blood in a potential flow under the additional assumption that heat is exchanged between blood and tissue only through capillaries [20]. In reality, a major part of heat exchange will occur through stronger blood vessels – a topic, which is presently under investigation.

A more realistic model is based on a *nonlinear* version of the BHT equation taking into account that blood flow depends on tissue temperature. Experiments [18] have shown that the blood flow in normal tissues, e.g., skin and muscle, increases significantly when heated up to $41-43°$C, whereas in the tumor zone the blood flow decreases with temperature. On this experimental basis, we chose $W = W(T)$ monotonically increasing in muscle and fat tissue, but monotonically decreasing in tumor tissue (for details see [13]).

Optimization Algorithm. In the following we focus on the stationary BHT equation. In a hyperthermia treatment the steady state is typically reached after 20 - 30 minutes and maintained for 40 - 60 minutes.

Our goal is to control the complex amplitudes z_j such that an effective hyperthermia therapy is achieved. In medical terms, a favorable temperature distribution is characterized as follows:

- within the tumor a therapeutic temperature level $T_{th} \approx 43°$C should be maintained,
- regions of healthy tissue should not be heated above $T_h \approx 42°$C,
- temperature in healthy tissue should not exceed certain limits T_{lim} depending on the tissue type: 42^oC for more sensitive tissue compartments (like bladder, intestine) and 44^oC otherwise.

From this we arrive at the objective function

$$f(p) = \int\limits_{\substack{x \in V_{tumor} \\ T(x,p) < T_{th}}} (T_{th} - T(x,p))^2 \, dx \; + \int\limits_{\substack{x \notin V_{tumor} \\ T(x,p) > T_h}} (T(x,p) - T_h)^2 \, dx \qquad (3)$$

to be minimized subject to the constraint

$$T(x,p) \leq T_{lim}(x) \,, \quad x \notin V_{tumor} \,.$$

where $p = \{\Re\, z_j, \Im\, z_j\}$ denote the control parameters.

In the *linear* heat transfer model superposition of the electric field $\mathbf{E}$ into k modes can be employed, which in $Q_e \sim \mid \mathbf{E} \mid^2$ leads to k^2 basic modes to be computed in advance, plus one further mode for the basal temperature T_{bas}.

In the *nonlinear* case, we construct some (cheap) fixed point iteration in terms of perfusion iterates W^m corresponding to iterates p^m.

optimization algorithm for the nonlinear BHT equation:

***k* Maxwell solves:** $\mathbf{E}^j(x)$ per channel $j = 1, \ldots, k$

superposition $\mathbf{E}(x) = \sum\limits_{j=1}^{k} z_j \mathbf{E}^j(x) \;,\; z_j \in \mathbb{C}$

control parameters $p = \{\Re\, z_j, \Im\, z_j\}$

$Q_e(x) = \frac{1}{2}\sigma(x) \mid \mathbf{E}(x) \mid^2 = \frac{1}{2}\sigma(x) \sum\limits_{j,l=1}^{k} \gamma_{jl}(p)\, \overline{\mathbf{E}}^j(x)\, \mathbf{E}^l(x)$

$\gamma_{jl}(p) \in \mathcal{P}_2(p)$

for $m = 0, 1, \ldots, n$: given p^m

one *nonlinear* BHT solve for $\mathbf{E}(p^m)$

supplies iterates T^m and $W^m = W(T^m)$

k^2 + 1 *linear* BHT solves with W^m:

$T^m_{bas}(x),\; T^m_{jl}(x)$ from $\frac{1}{2}\sigma(x)\overline{\mathbf{E}}^j(x)\mathbf{E}^l(x) \quad j,l = 1, \ldots, k$

superposition $T(x,p,W^m) = T^m_{bas}(x) \; + \sum\limits_{j,l=1}^{k} \gamma_{jl}(p)\, T^m_{jl}(x)$

$T(x,p,W^m) \;\in\; \mathcal{P}_2(p)$

$f(p) \;\in\; \mathcal{P}_2(T) \;\in\; \mathcal{P}_4(p)$

optimization $f(p) = min$ supplies p^{m+1}

The above fixed point iteration exploits the fact that the Maxwell solves are considerably more expensive than the BHT solves. It converges fast with an observed contraction factor of $\theta \approx 0.3$. In the *nonlinear* case the total computational cost is then

$$\begin{aligned} cost_{total} \;\; = \;\; & k * cost_{Maxwell} + \\ & n * (cost_{nlBHT} + (k^2+1) * cost_{lBHT} + cost_{Opt}) \end{aligned} \qquad (4)$$

where the notation $cost_{Maxwell}$, $cost_{nlBHT}$, $cost_{lBHT}$ and $cost_{Opt}$ is self-explaining. In typical computations we need about $n \approx 6$ optimization iterations. In the *linear* case the total cost is reduced to

$$cost_{total} = k * cost_{Maxwell} + (k^2 + 1) * cost_{lBHT} + cost_{Opt} \tag{5}$$

The Maxwell solver will be described in Section 3 below. For the linear BHT equation we apply the additive multilevel algorithm KASKADE [4, 8]. For the nonlinear BHT equation, the algorithm KARDOS [13] has been selected.

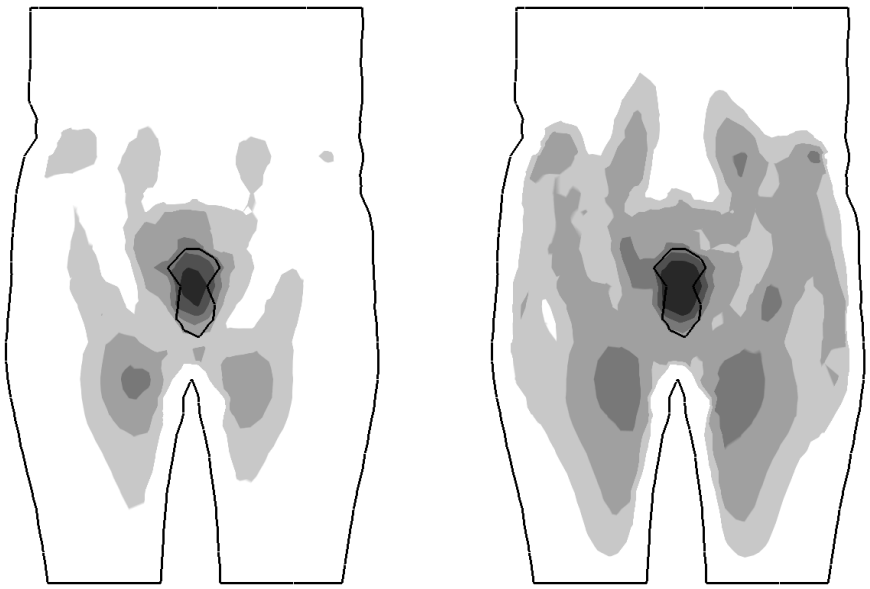

Figure 1: *Optimized temperature distributions in a frontal section of the pelvic region, based on the linear model (left) and the nonlinear model (right). Black lines: body outline and tumor contour. Light grey to dark grey: regions heated above* 39°C *to* 43°C.

Model Comparison. Our simulations show significant qualitative differences between the temperature distributions predicted by the linear and the nonlinear heat transfer model, as illustrated in Fig. 1. Generally speaking, the self–regulation of healthy tissue reflected by the nonlinear model reduces "hot spots" caused by local maxima of the absorbed electromagnetic fields. This is one reason for a slightly better tumor heating (ca. 0.5°C) predicted by the nonlinear model. An analogous result is reported in [19] for ferromagnetic thermoseed hyperthermia. An important finding is that the nonlinear model has an impact on the optimal treatment parameters as well. Maximal discrepancies turned out to be 22° for the phases θ_j and 0.22 for the relative amplitudes a_j. See [13] for a more detailed discussion.

3 Electromagnetic Field Computations

As mentioned above, the electromagnetic field computations (Maxwell solves) dominate the numerical work – which, by the way, itself is dominated by the segmentation work (compare Table 3).

Finite Element Formulation. As the hyperthermia applicator is working with a fixed angular frequency ω, our field computations are based on the time-harmonic Maxwell's equations. The electric and magnetic fields $\mathcal{E}$ and $\mathcal{H}$ have the representation $\mathcal{E}(\mathbf{x},t) = Re\,\mathbf{E}(\mathbf{x})e^{i\omega t}$, $\mathcal{H}(\mathbf{x},t) = Re\,\mathbf{H}(\mathbf{x})e^{i\omega t}$, where $\mathbf{E}(\mathbf{x})$ and $\mathbf{H}(\mathbf{x})$ are complex amplitudes defined on a computational domain $\Omega \subset \mathcal{R}^3$.

In our application we are dealing with linear isotropic dielectric media without free charges. We start with the well-known double-curl equations for the electric field $\mathbf{E}$

$$\mathbf{curl}\,\frac{1}{\mu}\mathbf{curl}\,\mathbf{E} - \omega^2\epsilon\mathbf{E} \;=\; 0\,, \tag{6}$$

where μ is the permeability and $\epsilon = \epsilon' - i\sigma/\omega$ represents a complex dielectric constant related to the generic dielectric constant ϵ' and the conductivity σ. For the current density $\mathbf{j}$, Ohm's law $\mathbf{j} = \sigma\mathbf{E}$ can be assumed.

Homogeneous Dirichlet boundary conditions for the tangential components of $\mathbf{E}$ define the metallic surfaces of the antennas, where a perfectly conducting material is assumed. Nonhomogeneous Dirichlet conditions are applied at the central antenna gaps, representing a prescribed voltage of the power generators. The computational domain of interest consists of a sphere covering patient model, water bolus and antenna array. On the surface of this sphere Sommerfeld-type conditions according to [12] are applied. They preserve both sparsity and symmetry properties of the finite element matrices.

According to the differential operator in (6), an appropriate space for the desired solution, which accomodates the Dirichlet boundary conditions (stated as $\mathbf{E}_t = \mathbf{E}_t^0$ on Γ_D) is given by

$$H_{\Gamma_D}(\mathbf{curl}\,,\Omega) := \{\mathbf{w} \in (L^2(\Omega))^3\,;\;\; \mathbf{curl}\,\mathbf{w} \in (L^2(\Omega))^3,\;\mathbf{w}_t = \mathbf{E}_t^0 \text{ on } \Gamma_D\}\,.$$

The related space for homogeneous boundary conditions $\mathbf{w}_t = 0$ will be denoted by $H_{\Gamma_D;0}(\mathbf{curl}\,,\Omega)$. In this space, a variational formulation for the desired field $\mathbf{E}$ reads: Find $\mathbf{E} \in H_{\Gamma_D}(\mathbf{curl}\,,\Omega)$ such that for all $\mathbf{w} \in H_{\Gamma_D;0}(\mathbf{curl}\,,\Omega)$

$$\int_\Omega \{\frac{1}{\mu}\mathbf{curl}\,\mathbf{E}\,\mathbf{curl}\,\mathbf{w} \;-\; \omega^2\epsilon\mathbf{E}\,\mathbf{w}\}\,d\Omega \;-\; \int_{\Gamma_{ext}} \beta(\mathbf{n}\times\mathbf{E})\,(\mathbf{n}\times\mathbf{w})\,d\Gamma \;=\; 0\,. \tag{7}$$

The second integral describes a contribution on the exterior surface, where $\beta > 0$ is related to the wave vector of the outgoing field (see [12]). Observe that for non-vanishing σ the bilinear form occurring in (7) is coercive and the problem has a unique solution (cf. e.g. [7]).

To obtain a conforming finite element discretization for (7), we generate a tetrahedral triangulation $\mathcal{T}_h$ of our domain and employ Nédélec's **curl**–conforming finite elements of lowest order [15], also called Whitney 1-forms or edge elements [5]. For a vector field $\mathbf{E}$ the degree of freedom $\mathbf{E}_e$ associated with each edge e in $\mathcal{T}_h$ is given by the path integral

$$\mathbf{E}_e = \int_e \mathbf{E}\cdot\mathbf{t}\,ds \tag{8}$$

along the edge e with tangent vector $\mathbf{t}$. The convergence behaviour of such discretizations for (7) is studied in [14].

Edge elements possess several distinct advantages: they guarantee the desired continuity of the tangential components of the electric field and are well-suited to suppress unwanted spurious modes [6]. Concave metallic edges and internal boundaries between materials with jumps in the coefficients can be incorporated in agreement with the physical continuity relations of the fields.

An outstanding feature becomes apparent with regard to the nullspace of the **curl**-operator. In terms of physics, this nullspace comprises irrotational fields which can be written as gradients of potentials. Whenever a vector field $\mathbf{E}_h$ is given in the Nédélec space ND_h on the triangulation $\mathcal{T}_h$, then its irrotational part $\mathbf{E}_p$ is the gradient of a discete potential Φ_h, *with* Φ_h *lying in the space of piecewise linear continuous finite element functions* S_h *on* $\mathcal{T}_h$. Thus for $\mathbf{E}_h \in ND_h$ we obtain a discrete Helmholtz decomposition

$$\mathbf{E}_h = \mathbf{E}_{h_p} + \mathbf{E}_{h_s}\,,\ \mathbf{E}_{h_p} = \mathbf{grad}\,\Phi_h \text{ with } \Phi_h \in S_h\,,$$

where $\mathbf{E}_{h_s}$ denotes the solenoidal part of $\mathbf{E}_h$ (for a detailed description we refer to Hiptmair [11] and Beck et al. [2]. This decomposition with directly accessible potentials Φ_h is of crucial importance for the construction of efficient solvers for the arising linear systems.

Linear System Solution and Multilevel Preconditioning. The variational formulation (7) yields a sparse linear equation system $A\mathbf{u} = \mathbf{b}$ with complex symmetric and indefinite matrix A. Due to Nyquist's theorem, typical "coarse" grids in our virtual patient models already comprise approximately 100,000 degrees of freedom.

Considering the bilinear form in (7), it is apparent that the nullspace $\mathbf{grad}\,S_h$ of the **curl**-operator is shifted to eigenvalues with negative real part. This is also the case for a certain (typically much smaller) number of modes in its orthogonal complement $ND_h^{\perp}$ with respect to ND_h. Since the dimension of the nullspace is quite "large", an iterative solver should provide means for tackling the modes within this space, which are inaccessible to standard smoothers.

As a basic solver we use the conjugate residual (CR) method, which is similar to the well-known conjugate gradient algorithm, but adjusted to symmetric indefinite systems [10]. For preconditioning we set up a hybrid smoothing procedure, whose prerequisites are analyzed in detail in [2, 3]. Its basic operations are Gauss-Seidel sweeps both in the Nédélec space ND_h, coping with the elliptic part of A, and in the nullspace. Within this framework, efficient transfer operators between field representations in S_h and ND_h are essential.

If we represent a vector field $\mathbf{E}_{h_p}$ in the nullspace by $\mathbf{E}_{h_p} = \mathbf{grad}\,\Phi_h$, then the representation in ND_h can be obtained easily from (8):

$$\mathbf{E}_e = \int_{P_1}^{P_2} \mathbf{grad}\,\Phi_h \cdot \mathbf{t}\,ds \;=\; \Phi_h(P_2) - \Phi_h(P_1)\,.$$

Here P_1 and P_2 denote the positions of the endpoints of the edge e.

In the follwing P_{S_h} denotes the transfer operator from the potential space S_h into the Nédélec space ND_h on $\mathcal{T}_h$. $P_{S_h}^*$ will denote the adjoint operator,

defining the canonical restriction. Then the smoother A_S for the nullspace is constructed by the Galerkin product $A_S = P_{S_h}^* A P_{S_h}$. The following hybrid smoothing algorithm for a given right hand side vector $r \in ND_h$ will provide an updated solution vector $u \in ND_h$ via the following steps:

(1) One Gauss-Seidel step for $Au = r$
(2) $\tilde{r} \leftarrow r - Au$
(3) $r_S \leftarrow P_{S_h}^* \tilde{r}$
(4) $u_S \leftarrow 0$
(5) One Gauss-Seidel step for $A_S u_S = r_S$
(6) $u \leftarrow u + P_{S_h} u_S$

In order to obtain a symmetric preconditioner, a subsequent step of the adjoint procedure has to applied. Note that both spaces are treated in a "multiplicative" fashion (speaking in terms of domain decomposition methods). As an alternative, we propose a symmetric additive version:

(1) One symmetric Gauss-Seidel step for $Au = r$
(2) $r_S \leftarrow P_{S_h}^* r$
(3) $u_S \leftarrow 0$
(4) One symmetric Gauss-Seidel step for $A_S u_S = r_S$
(5) $u \leftarrow u + P_{S_h} u_S$

If we employ adaptive mesh refinement, thus creating a sequence of nested triangulations $\mathcal{T}_0 \subset \mathcal{T}_1 \subset \ldots \subset \mathcal{T}_h$, the extension to a multilevel solver is quite straightforward. Taking into consideration that the associated sequence of Nédélec spaces is nested, i.e. $ND_0 \subset ND_1 \subset \ldots \subset ND_h$, we may adopt the classical multigrid idea [9] by using canonical grid transfer operations between these spaces, but employing a hybrid smoother on each level. Now the basic CR algorithm is preconditioned by one multiplicative V-cycle within each iteration. For detailed examinations of its convergence behaviour we refer to [2].

To assess the efficacy of our algorithmic concept, we present an example from our applications. As Table 1 shows, the solvers with hybrid smoothing exhibit a superior performance and do not deteriorate with increasing refinement level. Note that we have no direct factorization available on the coarse grid, thus facing comparatively large iterations counts. A proof of optimal multigrid complexity of this type of algorithm can be found in [2, 11].

Ref. Depth	Nodes	#Iter			CPU [min]		
		Std	M-Hyb	A-Hyb	Std	M-Hyb	A-Hyb
0	128 365	4250	354	413	150	24	20
1	373 084	4832	265	277	800	76	60
2	1 085 269	> 10000	186	194	> 2000	215	160

Table 1: *Convergence history for multilevel solvers with standard Gauss-Seidel* (Std)*, multiplicative* (M-Hyb)*, and additive* (A-Hyb) *hybrid Gauss-Seidel smoothing on each level. The iteration is terminated if the ratio of the euclidian norms of residual and right hand side is below* 10^5.

Adaptive Mesh Refinement. Due to the complex geometrical structure and strongly varying material properties of our finite element models, we consider adaptive mesh refinement to be of crucial importance to ensure both efficiency of our algorithm and reliability of our computational results.

For steering the local refinement, we employ a hierarchical local error indicator in the spirit of [8] which renders asymptotically correct error estimates in the case of self-adjoint problems [2]. As we are dealing with equations of partly hyperbolic nature in this context, it is clear that a local estimator cannot capture far-reaching field contributions so that we prefer here the term error indicator ([1]).

In order to obtain a hierarchical extension of the lowest-order edge element, we use basis functions as described in [17], including polynomials up to second order. If λ_i denotes the barycentric (i.e. linear Lagrangian) shape function associated with vertex i, then the vector basis function of the lowest order Nédélec space associated with edge $\{ij\}$ may be written as

$$\mathbf{w}^L_{\{ij\}} \;=\; \lambda_i \mathbf{grad}\,\lambda_j - \lambda_j \mathbf{grad}\,\lambda_i \;.$$

When adding the hierarchical surplus, we have one more degree of freedom on each edge

$$\mathbf{w}^H_{\{ij\}} \;=\; \lambda_i \mathbf{grad}\,\lambda_j + \lambda_j \mathbf{grad}\,\lambda_i$$

and two additional ones on each face (with vertices $i<j<k$) of the triangulation:

$$\mathbf{w}^{H,1}_{\{ijk\}} = \lambda_i\lambda_j \mathbf{grad}\,\lambda_k - \lambda_i\lambda_k \mathbf{grad}\,\lambda_j\,, \quad \mathbf{w}^{H,2}_{\{ijk\}} = \lambda_i\lambda_j \mathbf{grad}\,\lambda_k - \lambda_j\lambda_k \mathbf{grad}\,\lambda_i$$

For the discrete global problem we obtain an extended system

$$\left(\begin{array}{cc} A^{LL} & A^{LH} \\ A^{HL} & A^{HH} \end{array}\right)\left(\begin{array}{c} E^L \\ E^H \end{array}\right) \;=\; \left(\begin{array}{c} b^L \\ b^H \end{array}\right)\,, \tag{9}$$

where the superscript ^{H} denotes components of the hierarchical surplus. For the mere purpose of error indication, we solve (9) only approximately via a defect equation for the hierarchical components:

$$A^{HH}\,E^H \;=\; b^H \;-\; A^{HL}\,E^L\;. \tag{10}$$

An approximate solution of (10) may be obtained via one block-Jacobi step only (!), where it is essential to keep the 2×2-block-entries of both functions $\mathbf{w}^{H,l}_{\{ijk\}}$, $l=1,2$, attached to each face of the triangulation (see [2]) for details). At first glance, this block-Jacobi sweep appears critical, as the matrix contains negative eigenvalues and the related eigenmodes may be amplified. However, the modulus of all negative eigenvalues being comparatively small, these modes can be expected to give only minor contributions.

For the purpose of measuring field energy and discretization error, we define the following norm (asterisks * denote complex conjugates):

$$\|\mathbf{v}\|^2_E \;:=\; \int\limits_\Omega \{\frac{1}{\mu}\mathbf{curl}\,\mathbf{v}\,\mathbf{curl}\,\mathbf{v}^* \;+\; \omega^2\epsilon \mathbf{v}\,\mathbf{v}^*\}\,d\Omega + \int\limits_{\Gamma_{ext}} \beta(\mathbf{n}\times\mathbf{v})\,(\mathbf{n}\times\mathbf{v}^*)\;. \tag{11}$$

Table 2 gives the percentage of the relative discretization error

$$\eta \;=\; 100 \cdot \frac{\| \binom{E^L}{E^H} - \binom{E^L}{0} \|_E^2}{\| E^L \|_E^2}$$

for the different refinement levels.

Ref. Level	Nodes	η
0	128 365	10.1 %
1	373 084	4.96 %
2	1 085 269	2.54 %

Table 2: *Estimated discretization errors.*

4 Old versus New Hyperthermia Applicator

During the past ten years the applicator most frequently used for regional hyperthermia was the *Sigma-60* applicator of *BSD Medical Corp.*, Salt Lake City, Utah (see Fig. 2). This applicator consists of eight antennas arranged on a ring with 60 cm diameter. The antennas are grouped into $k = 4$ channels which can be independently controlled. The space between the antenna ring and the patient's body is filled with a so-called *water bolus* containing de-ionized water.

The new *Sigma-Eye* applicator (see Fig. 2), partly based on results of our simulations, was introduced in the beginning of 1998. It has 24 antennas (hence $k = 12$ channels) arranged in three parallel rings thus allowing for an additional power steering along the patient's axis. The much smaller bolus volume has an "eye"-shaped cross-section.

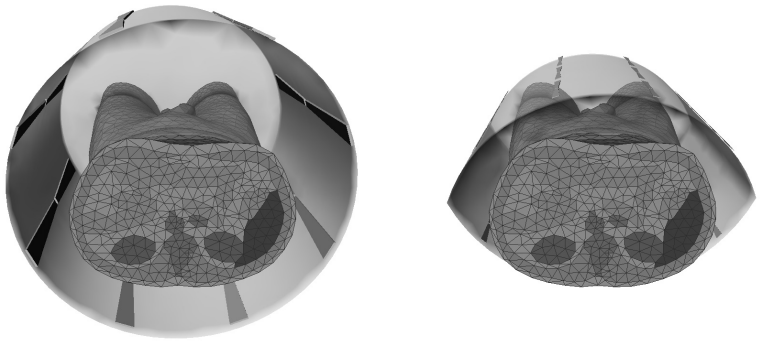

Figure 2: *Sigma-60 applicator (left) and Sigma-Eye applicator (right).*

In what follows we document some comparative results for both the old and the new applicator. Table 3 shows the computation times for the whole simulation process, based on the linear BHT as heat transfer model. Note that

the field calculation time per channel of the Sigma-Eye is about 10 minutes compared to about 20 minutes for the Sigma-60, essentially due to the smaller bolus volume. As explained in Section 2, the temperature calculation times roughly depend on k^2.

	Sigma-60 $k = 4$	Sigma-Eye $k = 12$
Segmentation	2 - 4 hours*	
Grid Generation	15 min**	
Field Calculation	80 min**	120 min**
Temperature Calculation	2 min**	20 min**
Optimization	6 sec**	1 min**
	* interactive ** CPU time (SUN UltraSparc)	

Table 3: *Computation times for the whole simulation process.*

Table 4 summarizes simulation results for three patients with typical tumor locations. Obviously, the new applicator significantly improves tumor heating in all cases while keeping 'hot spots' in healthy tissue at a constant level or slightly reducing them. The second location is the most difficult one since the tumor is to a large extent enclosed by bony structures.

	part of tumor volume heated to above 43°C	
	Sigma-60 (old)	Sigma-Eye (new)
distal (supraanal) rectal carcinoma	17.5%	62.5%
highly presacral rectal carcinoma	0.7%	18.4%
cervical carcinoma at pelvic wall	24.8%	49.1%

Table 4: *Comparison of old and new applicator for three patients with different tumor locations.*

5 Conclusion

The simulations reported herein are based on a *virtual patient* model that involves detailed individual geometry (patient, applicator, antennas) and correct electrical material properties, but only average values for the biological parameter perfusion. Even with this restriction, our simulations seem to be already helpful in the *decision*, whether regional hyperthermia is a promising modality for an individual patient. Beyond that, the developed methods also support the design of new applicator geometries and of new special purpose antennas.

Acknowledgements. The authors wish to thank Peter Wust from Virchow-Klinikum Berlin for his inspiring cooperation and Rudolf Beck for his input concerning the Maxwell multilevel solver. This work was supported by Deutsche Forschungsgemeinschaft, Sonderforschungsbereich 273 "Hyperthermie: Methodik und Klinik".

References

[1] I. Babuška, R. Durán, and R. Rodriguez. Analysis of the efficiency of an a posteriori error estimator for linear triangular finite elements. *SIAM J. Numer. Anal.*, 29, pp. 947-964, 1992.

[2] R. Beck, P. Deuflhard, R. Hiptmair, R.H.W. Hoppe, and B. Wohlmuth. Adaptive multilevel methods for edge element discretizations of Maxwell's equations. *ZIB Preprint SC 97-66.* To appear in *Surveys for Mathematics in Industry.*

[3] R. Beck and R. Hiptmair. Multilevel solution of the time-harmonic Maxwell equations based on edge elements. *ZIB Preprint SC 96-51.* To appear in *Int. J. Num. Meth. Eng.*

[4] F. Bornemann, B. Erdmann, and R. Kornhuber. Adaptive multilevel methods in three space dimensions. *Int. J. Numer. Meth. Engrg.*, 36, pp. 3187-3202, 1993.

[5] A. Bossavit. Whitney forms: a class of finite elements for three-dimensional computation in electromagnetism. *Inst. Elec. Eng. Proc., Part A*, 135, pp. 493-500(8), 1988.

[6] A. Bossavit. Solving Maxwell's equations in a closed cavity and the question of spurious modes. *IEEE Trans. Mag.*, 26(2, pp. 702–705), 1990.

[7] S. Caorsi and M. Raffetto. Electromagnetic boundary value problems in the presence of a partly lossy dielectric: considerations about the uniqueness of the solution. *IEEE Trans. Microwave Theory Tech.*, 44(8, pp. 1511-1513), 1996.

[8] P. Deuflhard, P. Leinen, and H. Yserentant. Concepts of an adaptive hierarchical finite element code. *IMPACT Comput. Sci. Engrg.*, 1, pp. 3-35, 1989.

[9] W. Hackbusch. *Multi-Grid Methods and Applications.* Springer, Berlin, 1985.

[10] W. Hackbusch. *Iterative Solution of Large Sparse Linear Systems of Equations.* Springer, Berlin, 1993.

[11] R. Hiptmair. *Multilevel Preconditioning for Mixed Problems in Three Dimensions.* Ph.D. Thesis, Wissner, Augsburg, 1996.

[12] V.N. Kanellopoulos and J.P. Webb. 3D finite element analysis of a metallic sphere scatterer: comparison of first and second order vector absorbing boundary conditions. *J. Phys. III France*, 3, pp. 563-572, 1993.

[13] J. Lang, B. Erdmann, and M. Seebass. Impact of nonlinear heat transfer on temperature control in regional hyperthermia. *ZIB Preprint SC 97-73.* Submitted to *IEEE Trans. Biomed. Engrg.*

[14] P. Monk. A finite element method for approximating the time–harmonic Maxwell equations. *Numer. Math.*, 63:243–261, 1992.

[15] J.C. Nédélec. Mixed finite elements in $\mathcal{R}^3$. *Numer. Math.*, 35, pp. 315-341, 1980.

[16] H.H. Pennes. Analysis of tissue and arterial blood temperatures in the resting human forearm. *J. Appl. Phys.*, 1, pp. 93-122, 1948.

[17] J.S. Savage and A.F. Peterson. High-order vector finite elements for tetrahedral cells. *IEEE Trans Microwave Theory Tech.*, 44(6, pp. 874-879), 1996.

[18] C.W. Song, A. Lokshina, J.G. Rhee, M. Patten, and S.H. Levitt. Implication of blood flow in hyperthermic treatment of tumors. *IEEE Trans. Biomed. Engrg.*, 31, pp. 9-16, 1984.

[19] D.T. Tompkins, R. Vanderby, S.A. Klein, W.A. Beckman, R.A. Steeves, D.M. Frey, and B.R. Palival. Temperature–dependent versus constant–rate blood perfusion modelling in ferromagnetic thermoseed hyperthermia: results with a model of the human prostate. *Int. J. Hyperthermia*, 10, pp. 517-536, 1994.

[20] P. Wust, J. Nadobny, R. Felix, P. Deuflhard, W. John, and A. Louis. Numerical approaches to treatment planning in deep rf-hyperthermia. *Strahlenther. Onkol.*, 165, pp. 751-757, 1989.